




# Electron spin resonance spectroscopic evidence of the transition to a spin-singlet state in the monomer Mott insulator (BEDT-TTF)Cu[N(CN)<sub>2</sub>]<sub>2</sub>

Muhammad Khalish Nuryadin <sup>1,\*</sup>, Yugo Oshima <sup>2</sup>, Naoki Yoneyama <sup>3</sup>, Satoshi Iguchi <sup>1</sup> and Takahiko Sasaki <sup>1,†</sup>

<sup>1</sup>*Institute for Materials Research, Tohoku University, Sendai 980-8577, Japan*

<sup>2</sup>*Meson Science Laboratory, RIKEN Cluster for Pioneering Research, Hirosawa 2-1, Wako, Saitama 351-0198, Japan*

<sup>3</sup>*Graduate Faculty of Interdisciplinary Research, University of Yamanashi, Kofu 400-8511, Japan*



(Received 31 August 2023; revised 11 January 2024; accepted 13 February 2024; published 8 March 2024)

(BEDT-TTF)Cu[N(CN)<sub>2</sub>]<sub>2</sub> (BEDT-TTF: bis(ethylenedithio)tetrathiafulvalene) is a monomer Mott insulator, in which the BEDT-TTF molecules form a three-dimensional (3D) distorted diamond structure; however, its physical properties resemble those of a quasi-one-dimensional (Q1D) zigzag BEDT-TTF chain structure. We investigated the magnetic ground state of this compound using electron spin resonance (ESR) spectroscopy in the X-band region (9.12 GHz) to confirm the occurrence of a transition to a spin-singlet state. The ESR spectra showed an asymmetric spectral line comprising two Lorentzian components, suggesting different correlations of the two independent 1D zigzag chains of the BEDT-TTF molecules. The spin susceptibility derived from the ESR spectra showed an opening of the spin gap below the transition temperature  $T_c \approx 25$  K possibly due to alternating intrachain interactions in both zigzag chains with different spin correlations.

DOI: [10.1103/PhysRevB.109.125115](https://doi.org/10.1103/PhysRevB.109.125115)

## I. INTRODUCTION

Organic salts based on bis(ethylenedithio)tetrathiafulvalene (BEDT-TTF, abbreviated as ET hereafter) are recognized as strongly correlated  $\pi$ -electron systems with flexible molecular arrangements, resulting in diverse physical properties [1]. Previously reported organic conductors based on ET salts, such as the  $\kappa$ -(ET)<sub>2</sub>X series, have a two-dimensional (2D) conduction layer of ET molecules with a 2:1 ratio of donor ET and anion X molecules, where  $X = \text{Cu}[\text{N}(\text{CN})_2]Y$  with  $Y = \text{Br}, \text{Cl}, \text{Cu}_2(\text{CN})_3$ , etc. These 2:1 ratio series of organic salts exhibit strong dimerization of the two ET molecules, changing from the quarter-filling band of ET molecules to an effective half-filling band of the dimers. Therefore, the bare Coulomb interaction  $U$  between the electrons in an ET molecule becomes an effective Coulomb interaction  $U_D$  in the dimer, often resulting in a dimer-Mott insulator [2]. To date, various studies have been conducted on dimer-Mott organic salts; however, ET organic salts with a 1:1 ratio between ET-to-anion molecules are rarely explored. Unlike the former ratio, the 1:1 ratio series or (ET)X salts have a formal charge of +1 from one site of the ET molecule, exhibiting a half-filled band. Therefore, (ET)X can generate a genuine Mott-insulating state with on-site Coulomb  $U$  values from the ET monomer site. To date, only a few (ET)X organic salts have been studied, including  $\zeta$ -(ET)PF<sub>6</sub> [3],  $\beta$ -(ET)TaF<sub>6</sub> [4], (ET)Ag<sub>4</sub>(CN)<sub>5</sub> [5,6], and (ET)Cu[N(CN)<sub>2</sub>]<sub>2</sub> [7], all of which are Mott insulators with specific ET arrangements.

Our focus has been on the recently studied (ET)Cu[N(CN)<sub>2</sub>]<sub>2</sub>, which contains a 1:1 ratio of donor ET<sup>+1</sup> (hole carrier) and anion Cu[N(CN)<sub>2</sub>]<sub>2</sub><sup>-1</sup> molecules.

Figure 1(a) shows the crystal structure in the (*ac*) plane, where the long axis of the ET molecules is tilted by approximately 20° with respect to the  $a^*$  axis. The title compound has a distinct ET arrangement compared with the other (ET)X series. The ET molecules are diagonally connected via intermolecular S-S contact with a transfer integral  $t$  to the nearest-neighbor molecules along the  $c$  axis and second-nearest-neighbor transfer integral  $t'$  to the other molecules, as shown in Fig. 1(b). These transfer integrals create one-dimensional (1D) ET chains and three-dimensional (3D) connections between the chains, which contain a columnar cavity occupied by polymeric anions. Therefore, as shown in Figs. 1(c) and 1(d), the ET molecules are located at the vertices of a distorted tetrahedron and its center, creating a distorted diamond structure.

In our previous study, a nodal line along the  $c$  axis was found in the band calculation, implying the viability of the title compound as a Dirac semimetal system [7]. However, the insulating transport results suggest an opening of the Mott gap at the nodal line, making the title compound a Mott-insulator material. As a result, the 3D distorted diamond structure of this system is transformed into a quasi-one-dimensional (Q1D) zigzag chain of ET molecules along the  $c$  axis with  $|t'/t| \approx 0.1$ . Interestingly, the static susceptibility reported in our previous study exhibits a sudden decrease below 25 K [7], which is attributed to the spin-singlet ground state. In contrast, (ET)Ag<sub>4</sub>(CN)<sub>5</sub>, another organic salt with a diamondlike structure, exhibits antiferromagnetic (AF) order at a transition temperature of  $T_N = 102$  K [5,6]. The other 1:1 ratios of  $\zeta$ -(ET)PF<sub>6</sub> and  $\beta$ -(ET)TaF<sub>6</sub> exhibit a spin-Peierls transition  $T_{SP} = 40$  K and AF order at  $T_N = 10$  K, respectively [3,4]. In another recent report, wire-shaped 1D (ET)Cu[N(CN)<sub>2</sub>]<sub>2</sub> exhibited a ferromagnetic transition at 13 K, and metallicity emerged owing to the strain effect resulting from molecular contact [8]. The spin-singlet magnetic ground state in the title

\*muhammad.khalish.nuryadin.e7@tohoku.ac.jp

†takahiko.sasaki.d3@tohoku.ac.jp

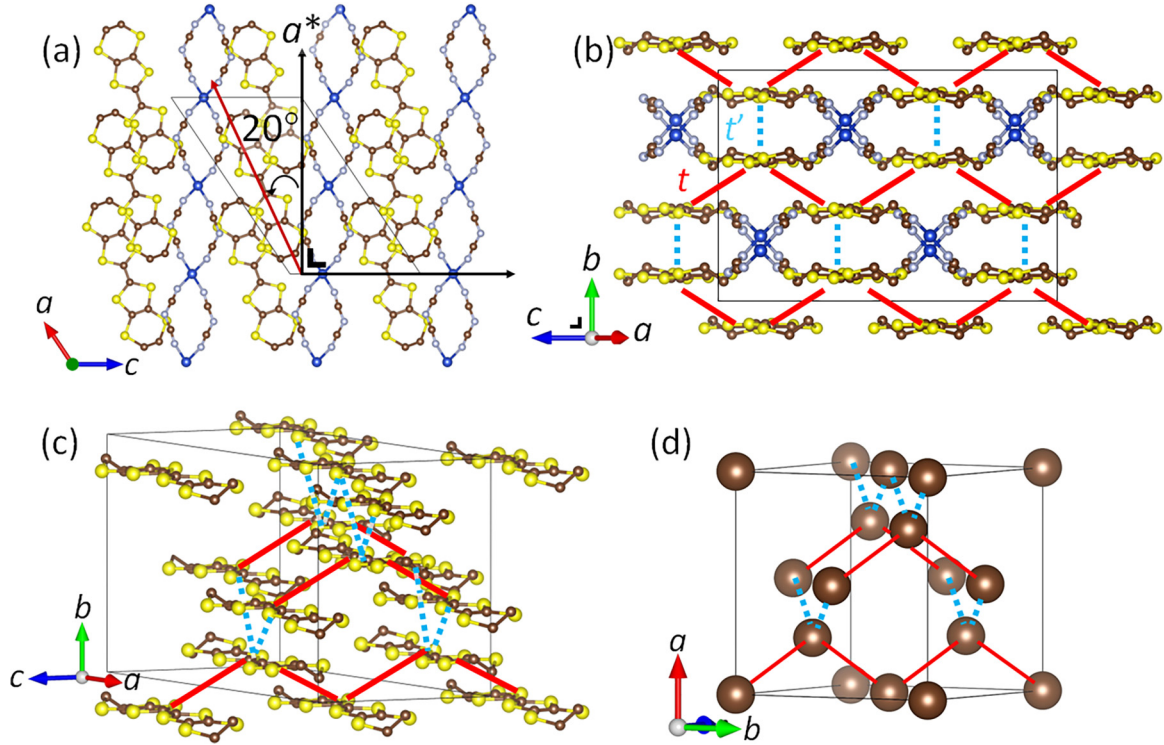


FIG. 1. (a) Crystal structure of  $(\text{ET})\text{Cu}[\text{N}(\text{CN})_2]_2$  viewed along the  $b$  axis. The long molecular axis of the ET molecules is tilted about  $20^\circ$  from the  $a^*$  axis, and the polymeric anion chain is oriented along the  $a + c$  axes. (b)  $(101)$  plane viewed along the anion chains showing the stacking of 1D ET zigzag chains via the transfer integral  $t$  and  $t'$ . The red solid and blue dotted lines correspond to  $t = -0.192$  eV and  $t' = 0.023$  eV, respectively [7]. (c) 3D arrangement view of the chain of ET molecules; the anions are omitted for simplicity. (d) Diamond lattice corresponding to the 3D arrangement shown in (c).

compound indicates that the electron pairs have symmetric orbital (and antisymmetric spin) wave functions, which contradicts the Mott-insulating state arising from the interaction of strong on-site Coulomb repulsion of one electron per lattice site. Therefore, despite the conflicting results, the existence of a variety of magnetic states indicates the importance of determining the magnetic ground state of  $(\text{ET})\text{Cu}[\text{N}(\text{CN})_2]_2$ .

In this study, we thoroughly investigated the magnetic ground state of  $(\text{ET})\text{Cu}[\text{N}(\text{CN})_2]_2$  via X-band electron resonance spin (ESR) spectroscopic measurements with angular and temperature dependence on a single crystal. Our findings showed that the magnetic ground state is a spin-singlet state with a transition temperature of 25 K. The possible mechanism for the spin-gap energy existing below the transition is analyzed using a 1D alternating Heisenberg spin chain, which has the two independent zigzag chains of ET molecules indicated by the appearance of isotropic  $g$ -value enhancement and linewidth broadening in ESR spectra. These two chains exhibit different spin correlations that are attributed to the change in ESR spectra from symmetric to asymmetric at 75 K, which is higher than the transition temperature of the spin-singlet state. Moreover, these two chains exhibit uniform exchange coupling in high-temperature regions.

## II. EXPERIMENTAL METHOD

Needlelike single crystals of  $(\text{ET})\text{Cu}[\text{N}(\text{CN})_2]_2$  were grown using the conventional electrochemical method reported by Wang *et al.* [9]. As previously reported [7], we

confirmed the  $C2/c$  space group and lattice parameters in a single crystal using x-ray structural analysis. Furthermore, there was almost no indication of a structural transition from 296 to 100 K.

ESR measurements were performed using a conventional X-band ESR spectrometer (JEOL JES-RE3X) with a magnetic field range of 319 to 326 mT equipped with a helium flow cryostat (Oxford Instruments). A single crystal with dimensions  $0.05 \times 0.05 \times 1.3$  mm<sup>3</sup> was mounted on a quartz rod. The angular dependence was determined by rotating the quartz rod relative to the crystal planes ( $a^*b$ ), ( $a^*c$ ), and ( $bc$ ) at 300 K to determine the principal axes of the  $g$ -value. Temperature dependence was measured on the principal axis of the  $g$ -value, which was relatively close to the  $a$  axis. Because the X-band ESR spectrometer uses the magnetic field modulation technique, the ESR spectrum appears as the first derivative of the ESR absorption, which provides three parameters from the line shape: peak-to-peak intensity  $I_{pp}$ , peak-to-peak linewidth  $\Delta H_{pp}$ , and resonance field  $H_0$ .

## III. RESULTS AND DISCUSSION

### A. Angular dependence of $g$ -value

Figure 2 shows the angular dependence of the  $g$ -value in the three crystallographic planes at room temperature. The  $g$ -value can be obtained using the relation  $g = h\nu/(\mu_B H_0)$ , where  $h$ ,  $\nu$ , and  $\mu_B$  represent the Planck's constant, frequency, and Bohr magneton, respectively. A magnetic field was applied with respect to the orthogonal axes  $a^*$ ,  $b$ , and  $c$ , which

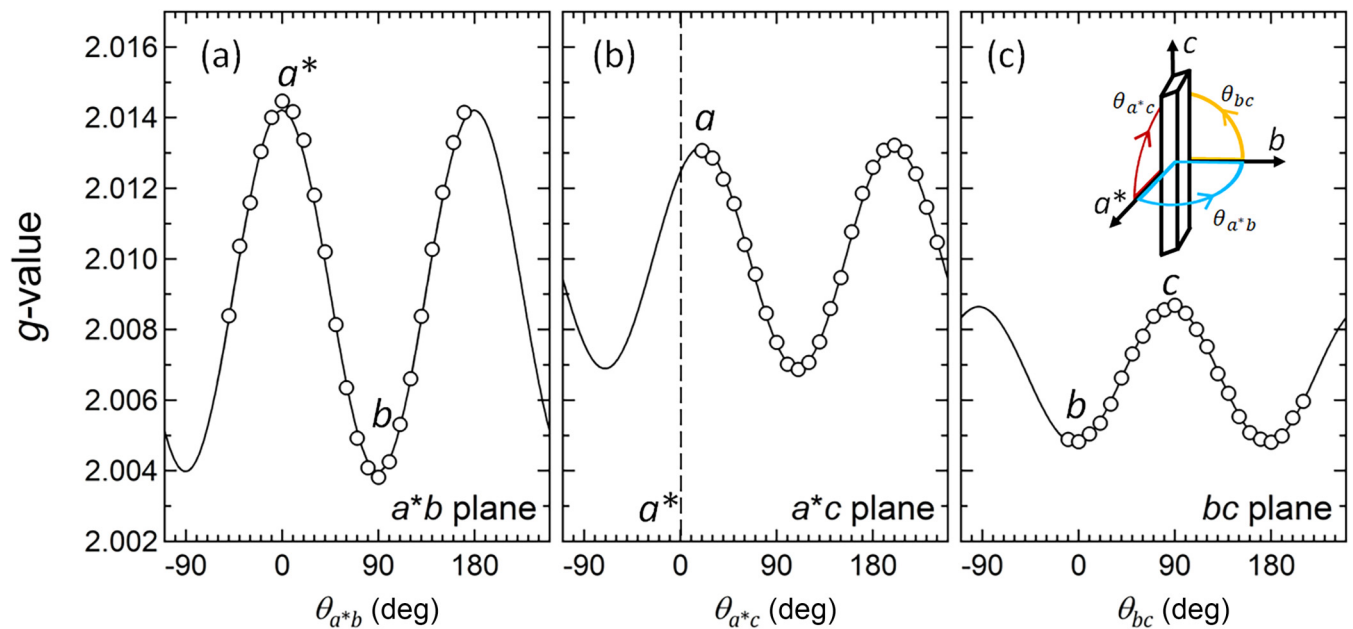


FIG. 2. Magnetic-field-direction dependence of  $g$ -value at 300 K in three different planes: (a) ( $a^*b$ ), (b) ( $a^*c$ ), and (c) ( $bc$ ). The black lines represent the fitting function of Eq. (1). Inset: Orthogonal axes  $a^*$ ,  $b$ , and  $c$ , assigned to the morphology of the needlelike crystal with rotational angles  $\theta_{a^*b}$ ,  $\theta_{a^*c}$ , and  $\theta_{bc}$ .

were assigned to the morphology of the needlelike crystals. The rotation axes were  $a^*$  to  $b$  ( $\theta_{a^*b}$ ),  $a^*$  to  $c$  ( $\theta_{a^*c}$ ), and  $b$  to  $c$  ( $\theta_{bc}$ ), as illustrated in the inset in Fig. 2. The  $g$ -values of the measured data were fitted using the following equation [10]:

$$g^2 = \sum_{i,j,k=a^*,b,c} g_{ij}g_{jk}l_i l_j, \quad (1)$$

where  $g$  and  $l$  are the  $g$ -value and cosine direction from the measured plane, respectively, according to the previously mentioned set of orthogonal axes. From the fitting results, the principal axes of the  $g$ -value with unit directional vector  $\vec{v}$  were  $g_{\max} = 2.0144$  with  $\vec{v} = (0.99, 0.004, -0.0171)$ ,  $g_{\min} = 2.0044$  with  $\vec{v} = (-0.004, 0.99, -0.0170)$ , and  $g_{\text{mid}} = 2.0086$  with  $\vec{v} = (0.0216, 0.0226, 0.99)$ . In addition, these values also contain information on the relationship between the morphology and the slight misalignment of the monoclinic crystals on the quartz rod.

The obtained  $g$ -value system was comparable to other ET-based organic salts. Sugano *et al.* previously determined the  $g$ -value of an ET molecule using ESR spectroscopy in  $\beta$ -(ET) $_2X$  ( $X = \text{I}_3$  and  $\text{IBr}_2$ ) [11]. According to their findings, the  $g$ -values follow the ET molecular symmetry, where  $g_{\max}$  is along the long axis of the molecule,  $g_{\min}$  is perpendicular to the plane of the molecule, and  $g_{\text{mid}}$  is along the short axis of the molecule. Another study on  $\kappa$ -(ET) $_2X$  showed similar  $g$ -value assignments interpreted from the molecular stacking geometry of the ET radical cation [12]. The assigned  $g$ -value of the title compound follows ET molecule orientation in the crystal, where the maximum and minimum  $g$ -values on the ( $a^*c$ ) plane are tilted by approximately  $20^\circ$  to the  $a^*$  axis. Therefore, the title compound is in good agreement with a previous study, which indicates that ESR measurements directly probe the  $\pi$  orbital of the ET molecule.

### B. Temperature dependence of the ESR spectra

Figure 3(a) shows the ESR spectra recorded at various temperatures in  $H \parallel a$ . The other directions show similar ESR spectra characteristics (i.e., isotropic characteristics) on their respective principal axes (see Supplemental Material [13]). A typical Lorentzian-type ESR spectrum of the radical ET molecules was observed at 300 K. As the temperature decreased from 300 to 25 K, the resonance field of the ESR spectra was nearly the same; however, the intensity gradually

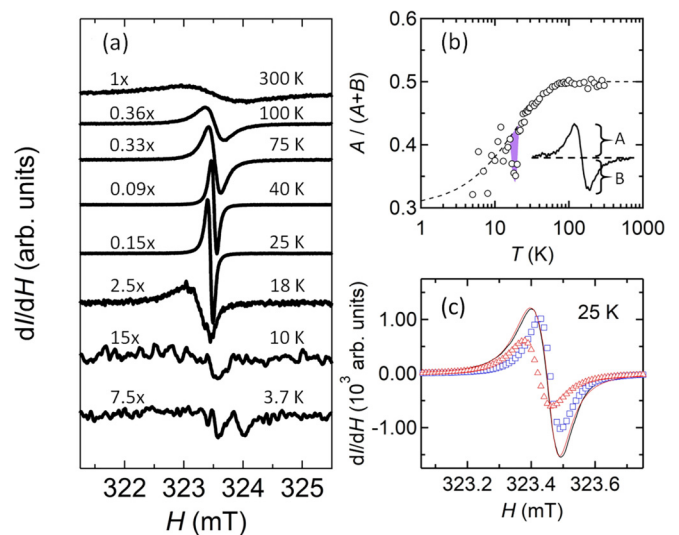


FIG. 3. (a) ESR spectra for  $H \parallel a$  from 300 to 3.7 K. (b) Temperature dependence of the  $A/(A+B)$  ratio (see inset). (c) Fitting results of Eq. (2) for the ESR spectrum at 25 K. The black line represents the experimental data, and the red line shows the sum of the two components 1 and 2 represented by squares and triangles, respectively.

increased and the spectral linewidth narrowed. Furthermore, the ESR spectrum began to weaken below 18 K, and two tiny signals with non-Lorentzian shapes were observed at 3.7 K. Interestingly, the ESR spectra also became asymmetric below 75 K, exhibiting an unusual line shape in which the upper peak was smaller than the bottom peak, contrary to the Dysonian line shapes typically found in other organic salts [11].

The spectral symmetry was determined by the ratio  $A/(A+B)$ , where  $A$  and  $B$  are the distances between the top and bottom peaks from the baseline, respectively [inset of Fig. 3(b)], and the ratio of 0.5 corresponds to a symmetric line shape. This ratio decreased exponentially from 75 to 25 K and started to decrease abruptly as a notch structure at approximately 18 K [violet area in Fig. 3(b)]. Below 10 K, the ratio was difficult to examine due to noise from the weak ESR signals and the appearance of two non-Lorentzian peaks. Similar temperature dependence of this behavior was observed in the other directions (see Supplemental Material [13]). Notably, the decrease in spectral symmetry begins at approximately 75 K, which is significantly higher than the transition temperature of 25 K reported in previous studies [7]. Furthermore, this asymmetric line shape cannot be explained by the skin-depth effect that typically appears due to the monotonic increase in conductivity [11].

The appearance of the non-Lorentzian ESR signals at 3.7 K suggests that the asymmetric ESR line shape below 75 K can be attributed to more than one ESR signal. The first derivative of the ESR signal with a Lorentzian line shape can be described using the following equation [14]:

$$\frac{dI}{dH} = \frac{16I_{PP}(H_0 - H)/(\Delta H_{PP}/2)}{[3 + \{(H - H_0)/(\Delta H_{PP}/2)\}^2]^2}. \quad (2)$$

The integrated intensity of the ESR absorption becomes  $(2\pi/\sqrt{3})I_{PP}\Delta H_{PP}^2$  from Eq. (2), which corresponds to the spin susceptibility  $\chi_s$ . Figure 3(c) shows a typical example of an asymmetric ESR signal fitted with two ESR components with Lorentzian line shapes. ESR components 1 and 2 are represented by the square and triangular symbols, respectively, in Fig. 3(c). The observed asymmetric ESR signal is clearly well reproduced by the sum of these two ESR components [red curve in Fig. 3(c)], where both components have equal integrated intensities but different linewidths. The field resonance difference between the two components is small, which implies that these components originate from the same spin states. Because the crystal has two zigzag ET chains [Fig. 1(b)], we conclude that the two Lorentzian components of the ESR spectra originate from the zigzag ET chains 1 and 2. Therefore, two Lorentzian components were fitted to the symmetric ESR spectrum with identical parameters to obtain continuity data from the low- to high-temperature regions. Although not observed in Fig. 3(a), an additional broad ESR signal with a large  $g$ -shift and broader ESR linewidth (in the range of 0.5 to 4 mT) appeared with sample-dependent characteristics (see Supplemental Material [13]). This additional component does not affect the primary ESR spectra and may originate from anionic magnetic impurities. Therefore, we focused on the two components that constitute the main ESR spectrum. Hereafter, the temperature dependence of  $H \parallel a$  is presented because the other principal axes exhibit similar behaviors (see Supplemental Material [13]).

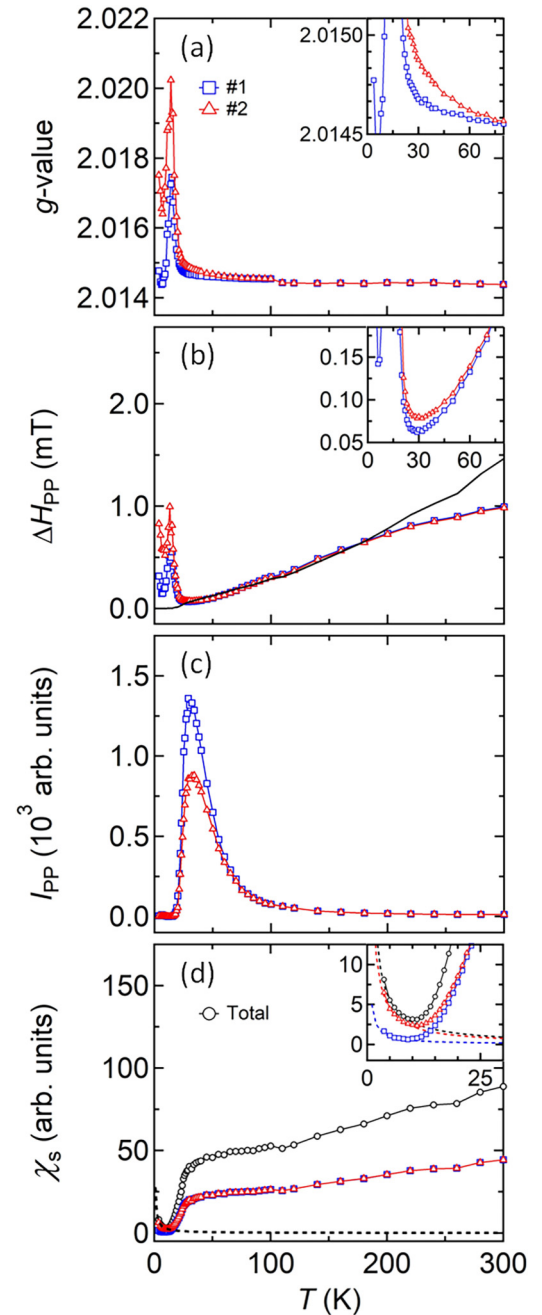


FIG. 4. Temperature dependence of the ESR parameters for  $H \parallel a$ : (a)  $g$ -value, (b)  $\Delta H_{PP}$ , and (c)  $I_{PP}$ . The square and triangular symbols represent the ESR parameters of components 1 and 2, respectively. (d) Integrated intensity  $\chi_s$  of components 1 and 2 and their total (circle). The black solid line in (b) corresponds to the 1D spin diffusion theory,  $\Delta H_{PP} \propto \chi_s T$ . The dashed lines in (d) correspond to the Curie component,  $\chi_C = C/T$ . Inset: Magnified view of  $g$ -value and  $\Delta H_{PP}$  below 75 K and integrated intensity  $\chi_s$  below 30 K.

### C. ESR parameters

Figure 4(a) shows that the  $g$ -values of components 1 and 2 remained mostly constant in the high-temperature regions. The  $g$ -values started to split and gradually increased, with minor differences below 75 K, as shown in Fig. 4(a). The  $g$ -values of components 1 and 2 abruptly increased below

25 K and peaked at 2.0173 and 2.0202 at 13 K, respectively. The  $g$ -value decreased to 10 K and then increased again to the lowest temperature of 3.7 K. The  $g$ -values of components 1 and 2 were 2.0148 and 2.0175 at 3.7 K, respectively. The appearance of the peak structure may indicate a change in the local internal field of the system at temperatures below 25 K. In addition, another signal was only visible at 3.7 K with a  $g$ -value of 2.0120, which may be due to the impurity spin after the complete disappearance of the internal field.

The  $g$ -shift in the 1D chain with the AF-ordered spin system occurs owing to the spin correlation of the short-range order and exhibits the anisotropic behavior of a negative  $g$ -shift only along the linear chain axis [15]. The positive  $g$ -shift was observed along the  $b$  axis in several  $\kappa$ -(ET)<sub>2</sub>X salt series, where the other directions show nearly temperature-independent behavior [12]. Moreover, this  $g$ -shift can be caused by the orientation changes in ET molecules, molecular orbital symmetry changes via the shortening of S-S contacts,  $\pi$ - $d$  exchange interactions, and AF instabilities. In contrast, the title compound shows an isotropic  $g$ -shift enhancement from the magnetically ordered phase below 25 K (see Supplemental Material [13]), indicating that the spin moment from the surroundings of spin correlations equals zero. The  $g$ -shift in the present study may not result from  $\pi$ - $d$  interactions as the anion molecule has a closed-shell orbital. This means that the  $g$ -shift in components 1 and 2 might indicate the presence of instabilities from the change in orientation and/or molecular orbital of the ET molecular chains with different spin correlations.

The temperature dependencies of  $\Delta H_{pp}$  and  $I_{pp}$  of the ESR spectra are shown in Figs. 4(b) and 4(c), respectively.  $\Delta H_{pp}$  of both components narrows linearly with decreasing temperature and starts to differ below 75 K, where component 2 is broader than component 1. After reaching a minimum at approximately 30 K, the linewidth rapidly increases below 25 K, exhibiting a peak structure with minimum and maximum values of 0.07 and 0.5 mT for component 1, and 0.09 and 1 mT for component 2. Next,  $\Delta H_{pp}$  increases again below 10 K, where the temperature dependence is similar to that of the  $g$ -value.  $I_{pp}$ , however, behaved differently from  $\Delta H_{pp}$ , as shown in Fig. 4(c). When the linewidth decreased to 30 K, the intensity showed a large peak structure in the same temperature region.  $I_{pp}$  of component 2 is approximately a quarter less than that of component 1 such that the integrated intensity of  $(2\pi/\sqrt{3})I_{pp}\Delta H_{pp}^2$  is essentially the same as that of component 1.

The linewidth depended on the type of spin interaction during the relaxation process. In a study of Mott insulators in ET organic salts, the narrowing of  $\Delta H_{pp}$  indicated a spin relaxation from the exchange interaction of the localized spin system [16]. Moreover, this narrowing can be explained by the theory of 1D spin diffusion via the spin-spin relaxation mechanism, wherein the spin diffusion at high temperatures is dominated by slowly decaying spin fluctuations following the relationship  $\Delta H_{pp} \propto \chi_s T$  [17]. Figure 4(c) shows that the linewidth follows this relationship above 25 K, but deviates above 200 K. Such a crossoverlike temperature dependence at around 200 K was also observed in the transport and static susceptibility results [7]. These results indicate thermal fluctuations caused by delocalized electrons via the spin-lattice

relaxation process. The spin relaxation process is affected by magnetic fluctuations from mixing different spin correlations between isolated electrons from  $g$ -values of components 1 and 2 below 25 K, resulting in broadened linewidths below the transition state.

Figure 4(d) shows the spin susceptibilities  $\chi_s$  of components 1 and 2 and their totals exhibit similar behaviors.  $\chi_s$  shows a monotonic decrease obtained by decreasing the temperature followed by a sudden drop at approximately 25 K. The monotonic decrease from high temperature in  $\chi_s$  might imply a uniform chain condition of the Bonner-Fisher (BF) model for the 1D Heisenberg AF spin-chain system, in which the exchange interaction  $J$  is approximately 500 K [7]. The sudden drop at  $T_c \approx 25$  K indicates a transition from a paramagnetic to a spin-singlet ground state. Moreover, the magnetic state change was supported by the occurrence of peaks in the  $g$ -value and  $\Delta H_{pp}$  below  $T_c$ , which can be seen in all directions. This spin-singlet pairing state is also shown in the other directions in terms of spin and static susceptibilities, wherein static susceptibilities show a sudden drop below  $T_c$  until 5 T (see Supplemental Material [13]).

The  $\chi_s$  value below 10 K increases as the temperature decreases, as shown in the inset in Fig. 4(d); these increased values are related to the Curie component  $\chi_C = C/T$  derived from the unpaired spins. The  $\chi_s$  total can be compared with the previously reported static susceptibility [7] to estimate the percentage of impurity spins, and the  $\chi_C$  values for component 1, component 2, and combined components are 0.02%, 0.08%, and 0.10%, respectively. Evidently, the impurity spin mainly originates from component 2, indicating that the spin densities of the two components differ. The next section will further explain the analysis of the energy gap after subtracting  $\chi_C$  from  $\chi_s$ .

#### D. Spin-gap energy analysis

Figure 5 shows the spin susceptibilities  $\chi_s^*$  obtained after subtracting the Curie component from the results described in the previous section, in which  $\chi_s^* = \chi_s - \chi_C$ , where  $\chi_{s1}^*$ ,  $\chi_{s2}^*$ , and  $\chi_{sTotal}^*$  are the component 1, component 2, and combined components, respectively. The spin-gap energy below  $T_c$  can be analyzed using the Arrhenius law, i.e.,  $\chi_s \propto \exp(-\Delta_E/T)$ . The fitting results, shown as dashed curves in Fig. 5, yield a similar energy gap of  $\Delta_E \approx 78$  K for all three susceptibilities, and this gap is slightly smaller than previously obtained from the static susceptibility ( $\Delta \approx 90$  K) [7]. Because  $\chi_s$  is derived from the well-aligned single crystal, the Curie contributions of the slightly different spins can be easily decomposed, and the corresponding results are more accurate than the static susceptibility derived from the sum of multiple Curie components from several single crystals. Therefore, this discrepancy in the spin gap can be ascribed to the error produced when  $\chi_C$  is subtracted from the static susceptibility.

The spin-gap energy can also be explained by the Bulaevskii model [18], which considers a 1D Heisenberg spin chain with an alternating AF interaction, represented by parameter  $\gamma$ , using the Hamiltonian

$$H = J \sum_n [\mathbf{S}_{2n} \cdot \mathbf{S}_{2n-1} + \gamma \mathbf{S}_{2n} \cdot \mathbf{S}_{2n+1}]. \quad (3)$$

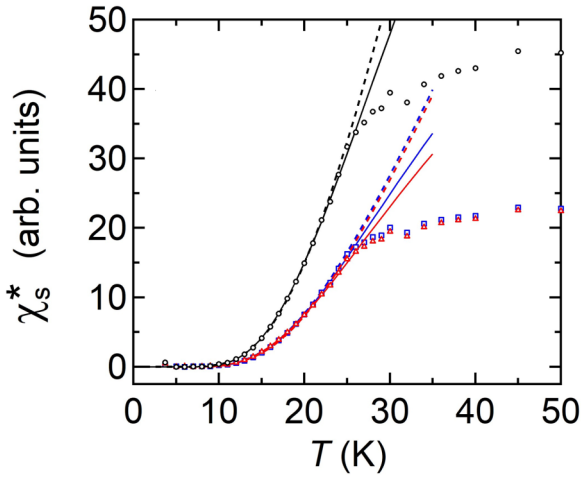


FIG. 5. Temperature dependence of the spin susceptibilities for component 1 ( $\chi_{s1}^*$ ), component 2 ( $\chi_{s2}^*$ ), and combined components ( $\chi_{sTotal}^*$ ) in  $H \parallel a$ , represented by the square, triangular, and circle symbols, respectively. The dashed lines correspond to the fitting results of the Arrhenius law, and the solid lines correspond to the Bulaevskii model with  $\gamma = 0.90, 0.92$ , and  $0.91$  for  $\chi_{s1}^*$ ,  $\chi_{s2}^*$ , and  $\chi_{sTotal}^*$ , respectively.

Here,  $\gamma$  is defined by the ratio of the two alternating couplings  $J_1$  and  $J_2$  ( $J_1 > J_2$ ) in the spin chain,  $\gamma = J_2/J_1$ . Further,  $\gamma = 0$  corresponds to the (strong) dimer model and  $\gamma = 1$  corresponds to a uniform spin chain. The spin susceptibility in the model can be expressed as

$$\chi_s = \frac{\alpha(\gamma)}{T} \exp\left[-\frac{J_1\beta(\gamma)}{T}\right], \quad (4)$$

where  $\alpha$  and  $\beta$  are functions of  $\gamma$ , and the values are adopted from a previously study [18]. Because  $\chi_s^*$  is in arbitrary units, the previous static susceptibility [7] was used to scale the obtained  $\chi_s^*$ . Then, the scaled data of  $\chi_s^*$  were divided by the factor  $N_A g^2 \mu_B^2 / k_B$  to make  $\chi_s^*$  unitless for the fitting procedure of Eq. (4), where  $N_A$  and  $k_B$  are the Avogadro number and Boltzmann constant, respectively. After that, the interpolation values  $\alpha(\gamma)$  and  $\beta(\gamma)$  from Bulaevskii's table [18] were used to determine  $J_1$  in the fitting process. The spin gap can be simply defined as  $J_1\beta(\gamma)$ . However, this energy gap can be further explained using other theories to obtain more information for this system. Pytte explained the dimerization of uniform spin chains into alternating chains based on the Peierls instability theory using the alternation parameter  $\delta$ , which can be derived from spin-phonon coupling [19]; here, the two unequal exchange couplings are defined as  $J_1 = J[1 + \delta(T)]$  and  $J_2 = J[1 - \delta(T)]$ . The parameter  $\delta(T) = (1 - \gamma)/(1 + \gamma)$  can be calculated based on the definition of  $\gamma$ , which becomes temperature independent below  $T_c$ . This implies that the energy gap between the singlet ground state and the spin-wave excited state below  $T_c$  can be considered to be the same as the conventional Peierls transition gap with  $2\Delta(T)$  [20,21]. Based on these theories, the spin energy gap may be represented as  $\Delta(T) = \delta(T)pJ$ , where  $p = 1.64$  [22].

The fitting results obtained using Eq. (4) are shown as solid curves in Fig. 5. The exchange couplings and their parameters for  $\chi_{s1}^*$ ,  $\chi_{s2}^*$ , and  $\chi_{sTotal}^*$  are shown in Table I. The

TABLE I. Fitting parameters used in Eq. (4) based on the Bulaevskii model.

$\chi_s^*$	$\gamma$	$\alpha(\gamma)$	$\beta(\gamma)$	$J$ (K)	$J_1$ (K)	$J_2$ (K)	$\Delta(T)$ (K)
No. 1	0.9	0.076	0.193	471	496	447	41
No. 2	0.92	0.0621	0.1573	561	585	538	38
Total	0.91	0.0692	0.1754	512	536	488	39

averaged energy gap is approximately  $\Delta(T) \approx 39$  K, where  $2\Delta(T) \approx J_1\beta(\gamma)$  are close to the Arrhenius gap. Moreover, the exchange coupling  $J$  of  $\chi_{sTotal}^*$  was comparable to the BF model of a uniform spin chain above  $T_c$ , as obtained in the previous static susceptibility analysis. Interestingly,  $\chi_{s1}^*$  and  $\chi_{s2}^*$  show different alternation parameters below  $T_c$ , indicating differences in their spin correlations. These results imply that the two independent zigzag chains formed a distorted diamond structure with uniform exchange coupling in the high-temperature region, and the couplings become different when the spin correlation is more dominant below  $T_c$ .

### E. Spin-singlet formation mechanism

The spin-singlet transition at  $T_c \approx 25$  K was confirmed using ESR measurements. The underlying mechanisms of spin-singlet formation in the high- and low-temperature phases are illustrated in Figs. 6(a) and 6(b), respectively. As mentioned previously, the ET molecules form two Q1D zigzag chains in the crystal. Figure 6(a) shows that intrachain exchange coupling is uniform in the high-temperature phase, resulting in symmetrical ESR spectra. This is supported by the BF-type spin susceptibility and linewidth narrowing of the 1D spin system [7,16]. The two chains gradually exhibit different spin correlations below 75 K, as indicated by the asymmetric ESR line shape as a precursor phenomenon, and the correlations become stronger close to  $T_c$ , as shown in the ESR parameters and Table I. The spins are dimerized in Fig. 6(b) due to the possibility of alternating exchange couplings  $J_1 - J_2$  existing along the intrachain, which might originate from the changes in molecular orbital symmetry via S-S contacts in the  $g$ -value enhancement. The differences in  $\chi_{s1}^*$  and  $\chi_{s2}^*$  indicate the different spin densities of the chains, where chain 1 has a nearly complete spin singlet and chain 2 has many impurity spins. This alternating chain can be formed via instabilities due to the interactions of the spin, charge, and orbital degrees of freedom [23]. Therefore, there are two possible scenarios for forming alternating chains in the crystal of the title compound.

One scenario for an alternating chain is the spin-Peierls transition due to the interaction between spins and dynamical phonons. In this case, the transition is well described by the relations of the BCS ratio  $2\Delta(0)/T_c = 3.53$  and the spin-lattice constant  $\lambda = T_c/0.8J$  [22], which are 3.18 and 0.058 in the present study, respectively. These values are comparable with those of other spin-Peierls materials [24–28]. This suggested the possibility of a spin-Peierls transition in the title compound.

Another scenario is the formation of an alternating chain due to charge disproportionation (CD) on the ET molecule, resulting in spin density ordering [29], as schematically shown

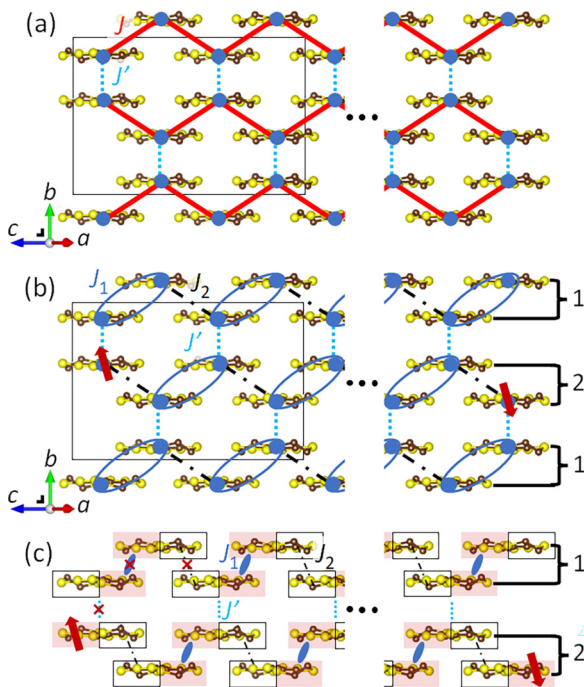


FIG. 6. (a) Spin-singlet mechanism based on the (101) plane. The 3D distorted diamond structure with exchange couplings  $J$  and  $J'$  is represented by the red solid and blue dotted lines, respectively. (b) Spin-singlet formation in the zigzag chains 1 and 2 with alternating coupling  $J_1 - J_2$  represented by the ovals and dash-dotted line for  $J_1$  and  $J_2$ , respectively. (c) Alternating chain based on the charge disproportionation scenario. The filled red and hollowed boxes correspond to the charge-rich and charge-poor halves, respectively. The X symbol represents the inversion center between two molecules.

in Fig. 6(c). When CD occurs, the charge-rich and charge-poor halves emerge in a molecule with different exchange couplings as represented by the red and hollow boxes in Fig. 6(c). In this scenario, the appearance of exchange differences can be understood naturally. However, this situation cannot occur because there is a twofold rotational axis located at the center of the ET molecule, which restricts the charge distribution between both sides. The inversion symmetry between the two molecules is irrelevant to the CD state. Therefore, breaking the twofold rotational symmetry allows for the CD state. Twofold rotational symmetry is easily broken by disorder in the anion arrangement via hydrogen bonds or the conformational degrees of freedom of the ethylene group of the ET molecules [30]. This situation might occur due to short contact distances

between the sulfur atom of the ET donor molecule and the carbon and nitrogen atoms of the anion molecule, which are less than the van der Waals distance, indicating that unfavorable strain exists in this compound [31].

Instability based on spin-Peierls and/or charge disproportionation scenarios can induce alternating chains that lead to the spin-singlet state. Although both scenarios require structural symmetry breaking, we did not observe an apparent change in the structural symmetry even below  $T_c$  through tentative synchrotron x-ray diffraction measurements conducted at the Photon Factory (PF), Institute for Materials Structure Science (IMSS), the High Energy Accelerator Research Organization (KEK), Tsukuba, Japan [32]. Examining the structure in detail is necessary to elucidate the spin-singlet state formation mechanism.

#### IV. CONCLUSIONS

In this study, the spin-singlet ground state in the monomer Mott insulator (ET)Cu[N(CN)<sub>2</sub>]<sub>2</sub> with  $T_c \approx 25$  K was microscopically confirmed by ESR spectroscopy. The temperature dependence of the ESR spectra line shape changed from symmetric to asymmetric below 75 K. The asymmetric spectrum consisted of two Lorentzian components originating from the two independent Q1D ET zigzag chains with different spin correlations. Although the two spin chains had different ESR parameters, both of the zigzag chains exhibited a spin-gap state below  $T_c$ . Analysis of the spin gap revealed a change in the exchange coupling from uniform  $J$  into alternating  $J_1$  and  $J_2$ . We discussed two possible scenarios, including the spin-Peierls transition and charge disproportionation in the ET monomer, to understand the spin-singlet formation in two different ET zigzag chains. However, further in-depth crystal structure analyses below 25 K are necessary to confirm the origin of the alternating spin-chain structure.

#### ACKNOWLEDGMENTS

We thank Shiori Sugiura, Daisuke Takahashi, Rie Haruki, and Reiji Kumai for their help in conducting the synchrotron x-ray structural experiments at Photon Factory (PF), Institute of Materials Structure Science (IMSS), High Energy Accelerator Research Organization (KEK), Tsukuba, Japan. This study was financially supported by the Japan Society for the Promotion of Science KAKENHI Grants No. 19H01833, No. 21H05471, No. 22H04459, No. 23H01114, No. 23K03271, No. 22H01149, and No. 23H04015.

[1] M. Dressel and S. Tomić, Molecular quantum materials: Electronic phases and charge dynamics in two-dimensional organic solids, *Adv. Phys.* **69**, 1 (2020).  
 [2] K. Kanoda and R. Kato, Mott physics in organic conductors with triangular lattices, *Annu. Rev. Condens. Matter Phys.* **2**, 167 (2011).  
 [3] H.-L. Liu, L.-K. Chou, K. A. Abboud, B. H. Ward, G. E. Fanucci, G. E. Granroth, E. Canadell, M. W. Meisel, D. R. Talham, and D. B. Tanner, Structure and physical properties of

a new 1:1 cation-radical salt,  $\zeta$ -(BEDT-TTF)PF<sub>6</sub>, *Chem. Mater.* **9**, 1865 (1997).  
 [4] T. Kawamoto, K. Kurata, T. Mori, and R. Kumai, A new genuine Mott insulator:  $\beta$ -(BEDT-TTF)TaF<sub>6</sub>, *J. Phys. Soc. Jpn.* **90**, 103703 (2021).  
 [5] Y. Shimizu, A. Otsuka, M. Maesato, M. Tsuchiizu, A. Nakao, H. Yamochi, T. Hiramatsu, Y. Yoshida, and G. Saito, Molecular diamond lattice antiferromagnet as a Dirac semimetal candidate, *Phys. Rev. B* **99**, 174417 (2019).

- [6] A. Otsuka, Y. Shimizu, G. Saito, M. Maesato, A. Kiswandhi, T. Hiramatsu, Y. Yoshida, H. Yamochi, M. Tsuchiizu, Y. Nakamura, H. Kishida, and H. Ito, Canting antiferromagnetic spin-order  $T_N = 102$  K in a monomer Mott insulator  $(\text{ET})\text{Ag}_4(\text{CN})_5$  with a diamond spin-lattice, *Bull. Chem. Soc. Jpn.* **93**, 260 (2020).
- [7] N. Yoneyama, M. K. Nuryadin, T. Tsumuraya, S. Iguchi, T. Takei, N. Kumada, M. Nagao, I. Tanaka, and T. Sasaki, Monomer Mott insulator  $(\text{BEDT-TTF})\text{Cu}[\text{N}(\text{CN})_2]_2$  as a potential nodal line system, *J. Phys. Soc. Jpn.* **91**, 113704 (2022).
- [8] Y. Huang, T. Mitchell, D. C. Yost, Y. Hu, J. B. Benedict, J. C. Grossman, and S. Ren, Emerged metallicity in molecular ferromagnetic wires, *Nano Lett.* **21**, 9746 (2021).
- [9] H. H. Wang, U. Geiser, J. M. Williams, K. D. Carlson, A. M. Kini, J. M. Mason, J. T. Perry, H. A. Charlier, and A. V. S. Crouch, Phase selectivity in the simultaneous synthesis of the  $T_c = 12.8$  K (0.3 kbar) organic superconductor  $\kappa$ - $(\text{BEDT-TTF})_2\text{Cu}[\text{N}(\text{CN})_2]\text{Cl}$  or the semiconductor  $(\text{BEDT-TTF})\text{Cu}[\text{N}(\text{CN})_2]_2$ , *Chem. Mater.* **4**, 247 (1992).
- [10] J. A. Weil and J. R. Bolton, *Electron Paramagnetic Resonance: Elementary Theory and Practical Applications* (Wiley, New York, 2007).
- [11] T. Sugano, G. Saito, and M. Kinoshita, Spin relaxation and diffusion in quasi-two-dimensional organic metals: The bis(ethylenedithio)tetrathiafulvalene compounds  $\beta$ - $(\text{BEDT-TTF})_2\text{X}$  ( $\text{X} = \text{I}_3$  and  $\text{IBr}_2$ ), *Phys. Rev. B* **35**, 6554 (1987).
- [12] T. Nakamura, T. Nobutoki, T. Takahashi, G. Saito, H. Mori, and T. Mori, ESR properties of  $\kappa$ -type organic superconductors based on BEDT-TTF, *J. Phys. Soc. Jpn.* **63**, 4110 (1994).
- [13] See Supplemental Material at <http://link.aps.org/supplemental/10.1103/PhysRevB.109.125115> for the details of ESR spectra along the three crystal axis directions, reproducibility of ESR spectra characteristics and parameters from a different sample, and static magnetic susceptibilities perpendicular and parallel to the  $c$  axis measured by the SQUID with various magnetic fields.
- [14] C. P. Poole and H. A. Farach, Line shapes in electron spin resonance, *Bull. Magn. Reson* **1**, 162 (1979).
- [15] K. Nagata and Y. Tazuke, Short range order effects on EPR frequencies in Heisenberg linear chain antiferromagnets, *J. Phys. Soc. Jpn.* **32**, 337 (1972).
- [16] N. Yoneyama, A. Miyazaki, T. Enoki, and G. Saito, Magnetic properties of TTF-type charge transfer salts in the Mott insulator regime, *Bull. Chem. Soc. Jpn.* **72**, 639 (1999).
- [17] Y. Ajiro, S.-i. Matsukawa, T. Yamada, and T. Haseda, Temperature dependence of the ESR line width in one-dimensional  $S = 1/2$  antiferromagnet  $\text{CuCl}_2 \cdot 2\text{NC}_5\text{H}_5$ , *J. Phys. Soc. Jpn.* **39**, 259 (1975).
- [18] L. N. Bulaevskaia, Magnetic susceptibility of a chain of spins with antiferromagnetic interaction, *Fiz. Tverd. Tela (Leningrad)* **11**, 1132 (1969) [*Sov. Phys. Solid State* **11**, 921 (1969)].
- [19] E. Pytte, Peierls instability in Heisenberg chains, *Phys. Rev. B* **10**, 4637 (1974).
- [20] D. Allender, J. W. Bray, and J. Bardeen, Theory of fluctuation superconductivity from electron-phonon interactions in pseudo-one-dimensional systems, *Phys. Rev. B* **9**, 119 (1974).
- [21] M. J. Rice and S. Strässler, Theory of a quasi-one-dimensional band-conductor, *Solid State Commun.* **13**, 125 (1973).
- [22] J. W. Bray, L. V. Interrante, I. S. Jacobs, and J. C. Bonner, The spin-Peierls transition, *Extend. Linear Chain Compounds* **3**, 353 (1983).
- [23] A. Vasiliev, O. Volkova, E. Zvereva, and M. Markina, Milestones of low- $D$  quantum magnetism, *npj Quantum Mater.* **3**, 18 (2018).
- [24] J. W. Bray, H. R. Hart Jr, L. V. Interrante, I. S. Jacobs, J. S. Kasper, G. D. Watkins, S. H. Wee, and J. C. Bonner, Observation of a spin-Peierls transition in a Heisenberg antiferromagnetic linear-chain system, *Phys. Rev. Lett.* **35**, 744 (1975).
- [25] I. S. Jacobs, J. W. Bray, H. R. Hart Jr, L. V. Interrante, J. S. Kasper, G. D. Watkins, D. E. Prober, and J. C. Bonner, Spin-Peierls transitions in magnetic donor-acceptor compounds of tetrathiafulvalene (TTF) with bisdithiolene metal complexes, *Phys. Rev. B* **14**, 3036 (1976).
- [26] S. Huizinga, J. Kommandeur, G. A. Sawatzky, B. T. Thole, K. Kopinga, W. J. M. de Jonge, and J. Roos, Spin-Peierls transition in  $N$ -methyl- $N$ -ethyl-morpholinium-ditetraacyanoquinodimethane  $[\text{MEM}(\text{TCNQ})_2]$ , *Phys. Rev. B* **19**, 4723 (1979).
- [27] M. Hase, I. Terasaki, and K. Uchinokura, Observation of the spin-Peierls transition in linear  $\text{Cu}^{2+}(\text{spin-1/2})$  chains in an inorganic compound  $\text{CuGeO}_3$ , *Phys. Rev. Lett.* **70**, 3651 (1993).
- [28] M. Dumm, A. Loidl, B. W. Fravel, K. P. Starkey, L. K. Montgomery, and M. Dressel, Electron spin resonance studies on the organic linear-chain compounds  $(\text{TMTCF})_2\text{X}$  ( $\text{X} = \text{S}, \text{Se}; \text{X} = \text{PF}_6, \text{AsF}_6, \text{ClO}_4, \text{Br}$ ), *Phys. Rev. B* **61**, 511 (2000).
- [29] E. Canévet, B. Grenier, Y. Yoshida, N. Sakai, L.-P. Regnault, T. Goto, Y. Fujii, and T. Kawae, Strong interplay between magnetic and structural properties in the spin-1/2 chain molecular compound  $\text{D-F}_5$  PNN, *Phys. Rev. B* **82**, 132404 (2010).
- [30] M. Pinterić, M. Čulo, O. Milat, M. Basletić, B. Korin-Hamzić, E. Tafra, A. Hamzić, T. Ivek, T. Peterseim, K. Miyagawa, K. Kanoda, J. A. Schlueter, M. Dressel, and S. Tomić, Anisotropic charge dynamics in the quantum spin-liquid candidate  $\kappa$ - $(\text{BEDT-TTF})_2\text{Cu}_2(\text{CN})_3$ , *Phys. Rev. B* **90**, 195139 (2014).
- [31] H. H. Wang, K. D. Carlson, U. Geiser, A. M. Kini, A. J. Schultz, J. M. Williams, U. Welp, K. E. Darula, V. M. Hitsman, M. W. Lathrop, L. A. Megna, P. R. Mobley, G. A. Yaconi, J. E. Schirber, and D. L. Overmyer, Syntheses and properties of  $\kappa$ -phase organic superconductors, *MRS Proc.* **247**, 471 (1992).
- [32] The crystal structure analysis by x-ray diffraction measurements at the Photon Factory (PF), Institute for Materials Structure Science (IMSS), and High Energy Accelerator Research Organization (KEK) shows the crystal symmetry at 20 K is the  $C2/c$  space group with lattice constants  $a = 16.6510$ ,  $b = 13.6294$ , and  $c = 10.2136$ . The symmetry  $C2/c$  below  $T_c$  is the same as the crystal structure at 300 K in Refs. [7,9].